Journal of Alloys and Compounds 1032 (2025) 181167

Contents lists available at ScienceDirect

Journal of Alloys and Compounds

journal homepage: www.elsevier.com/locate/jalcom

Oxidation and microstructure evolution of ODS-FeCrAl alloys under dynamic lead-bismuth eutectic

Jiwu Liu [a], Kun Yang [a,b,*], Wangwei Ru [a], Tianhao Liu [a], Zhangjie SUN [a], Feida Chen [a,b], Xiaobin Tang [a,b]

[a] Department of Nuclear Science and Technology, Nanjing University of Aeronautics and Astronautics (NUAA), Nanjing 211106, China
[b] Key Laboratory of Advanced Nuclear Technology and Radiation Protection, Ministry of Industry and Information Technology, Nanjing211106, China

ARTICLE INFO

Keywords:
FeCrAl alloy
Pb-Bi eutectic
Oxidation film
High temperature corrosion

ABSTRACT

The robustness of the surface oxidation film subjected to the dynamic flow of Pb-Bi eutectic is critical to the anti-corrosive ability of FeCrAl alloy. Herein, the microstructure evolution of oxide film of ODS-FeCrAl alloy has been investigated by both experimental and finite elemental modeling. Results indicate that the corrosion-generated oxide film featured with three distinct structural layers, which is thermodynamic driven: a magnetite layer, a Fe (Cr, Al) spinel layer, and an internal oxide layer, arranged from outermost to innermost. The unevenly distribution of the exterior magnetite layer can be attributed to the LBE scouring, corrosion dissolution, and oxidation. Dynamic LBE in the experiment has a substantial impact on the mechanical strength of the multilayer oxide film according to finite element simulation. The current study revealed the mechanical properties of the multi-layer oxide film subjected to LBE, with Al_2O_3 suffered the highest shear stress according to the FEA.

1. Introduction

Lead-cooled fast reactors, a type of reactor cooled with lead-bismuth eutectic (LBE), have emerged as one of the most promising fourth-generation reactor due to their high safety margin, and high power density [1–3]. Lead-bismuth eutectic (LBE: 44.5 wt% Pb; 55.5 wt% Bi), a promising coolant with a low melting point, high boiling point (1670 °C), low reactivity, high radiation resistance, and high thermal conductivity, not only improves the power density but also ensures the safety of the reactor, especially under LOCA scenario [4–6]. However, under the high-temperature LBE environment, the structural materials will face severe problems such as dissolution corrosion [7,8], oxidation behavior [9,10], and scratching corrosion [11–13], causing the so-called liquid metal-assisted corrosion (LME) [14–17], thus threatening the safe operation of LFR. Therefore, increase the structural material reliability through mitigating the lead-bismuth corrosion effect is of particular importance.

Ferritic alloy was pointed out to form a protective oxide layer in liquid LBE with balancing amount of oxygen which in turn can be recognized as a feasible strategy to mitigate or reduce the corrosion rate of structural material in LBE [18,19]. The dense oxide film formed on the surface in a high-temperature environment can effectively prevent the further erosion of liquid LBE, thus significantly extending the service life cycle of structural materials [20–26]. The ferritic/martensitic FeCrAl alloy displays a so-called “third element effect” (TEE), which can improve the bonding strength and adhesion of the film between the oxide film/metal matrix, reduce the risk of oxide film peeling in the presence of mechanical shear forces. Previous researches have pointed out that multiple layer oxide film, including Cr_2O_3 and Al_2O_3 gradually covered on the sample surface with their thickness strongly associated with the localized temperature (high-temperature steam or Pb/LBE), which further exhibits superior anti-corrosive ability [27–29]. Oxide dispersion strengthened ODS-FeCrAl alloys with rare earth (REs) and nano-oxides incorporated can inhibit the growth of dislocation through refining the grain size, has attracted growing attention [30]. Besides, the formation of surface oxide film enriched in aluminum oxide during high-temperature oxidation can improve the high-temperature oxidation resistance thus increasing the alloy’s reliability, especially under LOCA scenario [31,32].

So far, researchers have carried out a series of experimental studies on the corrosion behavior of FeCrAl alloy under oxygen-saturated condition [33,34] high-temperature steam [35,36], supercritical water [37,38], etc. The microstructure and growth kinetic of the oxide layers formed on the surface of FeCrAl alloys are highly depended on the

* Corresponding author at: Department of Nuclear Science and Technology, Nanjing University of Aeronautics and Astronautics (NUAA), Nanjing 211106, China.
E-mail address: kun.yang@nuaa.edu.cn (K. Yang).

https://doi.org/10.1016/j.jallcom.2025.181167
Received 12 February 2025; Received in revised form 28 April 2025; Accepted 22 May 2025
Available online 22 May 2025

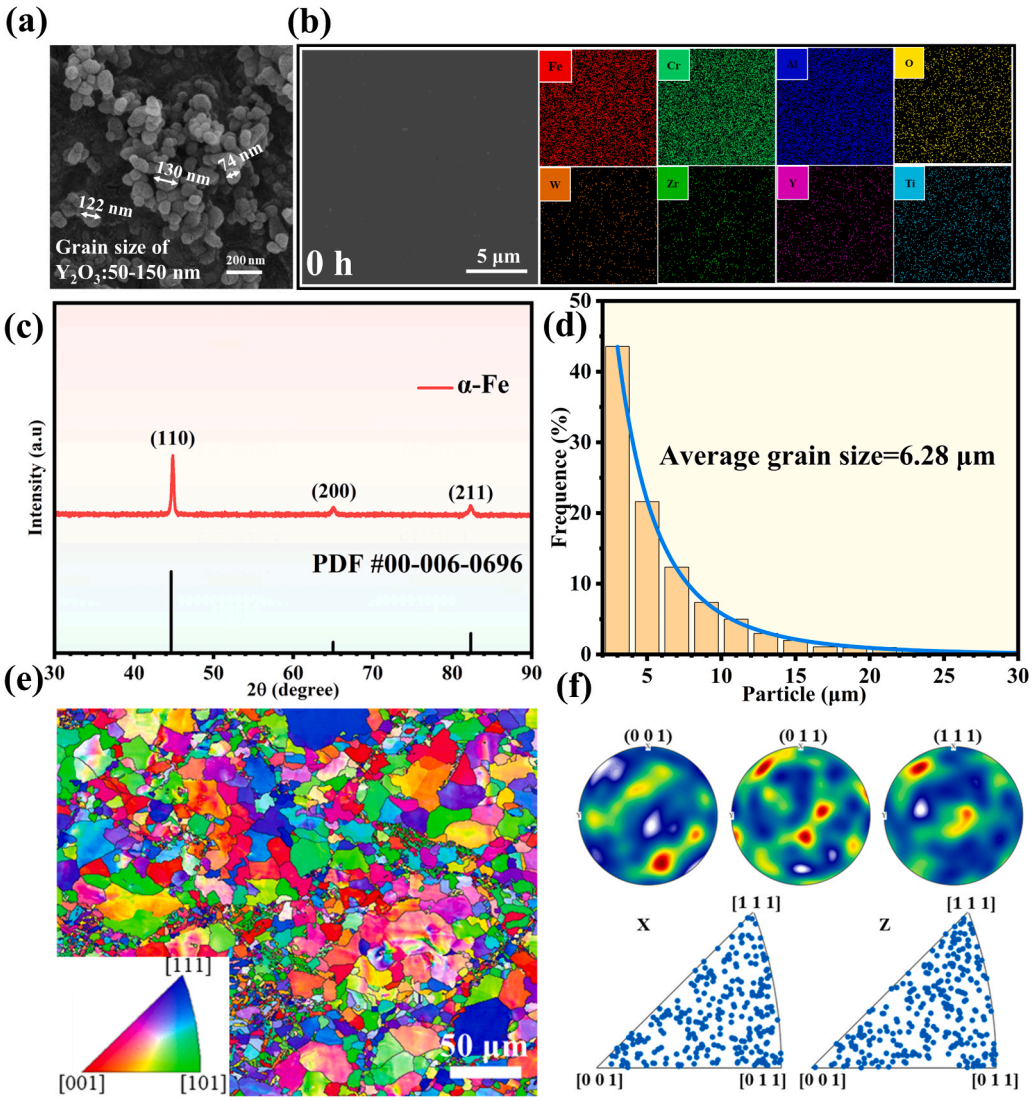

Fig. 1. (a) Grain size of nano sized Y_2O_3 particles; (b) elemental analysis of ODS-FeCrAl specimen before corrosion;(c) XRD spectra of ODS-FeCrAl samples before corrosion; (d) Grain size of ODS-FeCrAl specimens before corrosion;(e) (f) IPF-Y plots, polar and antipolar plots of ODS-FeCrAl specimen before corrosion.

temperatures and oxygen concentrations in LBE [39,40]. Compared with the static LBE corrosion environment, the mechanical behavior of the oxidation film subject to the dynamic flow of high-temperature LBE (simulate the reactor loop) was rarely studied. The corrosion behavior of alloys in dynamic lead-bismuth environments is often more severe than that in static lead-bismuth environments. The shear stress generated by the mechanical interaction between surface oxidation film and LBE can significantly accelerate the degradation of the oxide film, leading to the transition of the corrosion mechanism to dissolution [41–43]. However, the potential nexus among chemical composition, heterogeneity of the oxidation film, and anti-corrosion property subjected to dynamic LBE is not well understood. Finite element analysis (FEA) is a strong tool to fundamentally study the dynamic behavior and structure evolution of the oxide film subjected to LBE flow. The failure and fracture behavior of materials including Mg and Zr alloys have been studied by the FEA assisted by GTN model [44,45]. Nègre et al. studied the crack extension in aluminum welds by using the GTN model [46], while Nonn et al. carried out a GTN based numerical modeling of damage behavior of laser-hybrid weld to study its effect on deformation and failure [47].

The current study intends to focus on the revealing of the oxidation film structural evolution and mechanical behavior of ODS-FeCrAl alloy in dynamic LBE under controlled oxygen conditions (1×10^{-4} wt% ~5×10^{-4} wt%) at 550 °C. The surface alteration behavior and the oxidation film microstructure evolution were analyzed by X-ray diffraction (XRD), scanning electron microscopy (SEM), atomic force microscopy (AFM), electron backscattered diffraction (EBSD), and transmission electron microscopy (TEM). In addition, the oxide film growth and defoliation mechanism and the shear stress of different oxide films under dynamic lead-bismuth interaction was studied via finite elemental analysis. The experimental result, accompanied by the modeling result, not only provides an experimental basis for understanding the mechanical behavior of oxide films in complex flow environments, but also provides theoretical baseline for the future development of alloys by focusing on the surface oxide film.

Table 1
ODS-FeCrAl alloy composition.

Elements	Cr	Al	W	Zr	Ti	Y	Y_2O_3	Fe
wt%	13	4	2	0.6	0.4	0.1	0.6	Bal

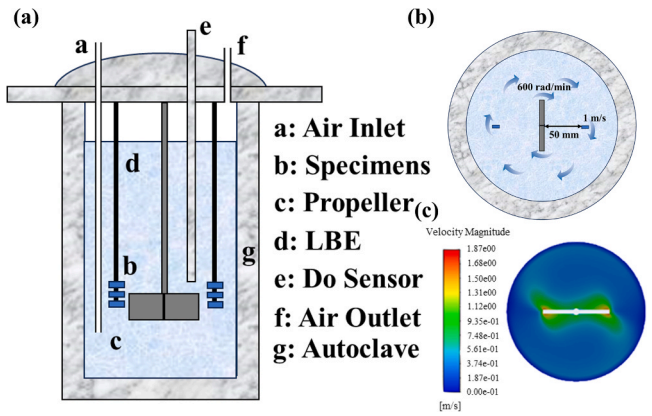

Fig. 2. (a) Schematic diagram of the dynamic LBE corrosion experimental equipment; (b) Top view of the experimental equipment; (c) LBE velocity profile of specimen surface simulated by Fluent.

2. Experiments

2.1. Material preparation

ODS-FeCrAl alloy with 0.6 wt% Y_2O_3 (50–150 nm, Fig. 1(a)) content was fabricated by high-energy ball milling (HEBM) combined with hot isostatic pressing (HIP) technique. The ODS-FeCrAl pre-alloyed powder (200 mesh) was ball milled with W powder (200 mesh), Zr powder (200 mesh), Ti powder (200 mesh), Y powder (200 mesh), and nanometer Y_2O_3 powder with a planetary ball mill (MITR-YXQM, Changsha MITR Co., Ltd.) following chemical composition as detailed in Table 1. The ball milling was carried out for 48 h under a high-purity argon atmosphere, with a milling speed of 300 r/min and a ball-to-powder ratio of 10:1. The samples were then consolidated using hot isostatic pressing (FHP-828 hot-press system Shanghai Hateng Co., Ltd.) at 1150 °C and 150 MPa for 2 h. The samples were cooled in the furnace at a rate of 5 °C/min to room temperature post sintering. The ODS-FeCrAl sample coupons, with the size of 10 mm× 10 mm× 5 mm, were prepared by cutting and manual grinding and then polished using SiC papers of grades 300, 600, 1000, 1500, 3000, and 5000. The sample coupons were then ultrasonically cleaned in acetone and ethanol and finally dried to obtain a smooth surface. After that, they were ultrasonically cleaned in ethanol for 10 minutes, rinsed with deionized water, and dried with nitrogen before further testing.

The microstructure and elemental distribution of the sample before corrosion is shown in Fig. 1(b). The flat surface without porosity suggests the highly densified structure achieved by hot-pressing. The corresponding elemental mappings show that Fe, Cr, and Al on the sample surface are uniformly distributed without segregation, suggesting the successful preparation of the sample coupon. The XRD patterns of ODS-FeCrAl alloys before the corrosion experiments are shown in Fig. 1(c). The main crystalline peaks can be indexed as Fe-Cr matrix without significant impurity crystalline phase being identified. The corresponding Y_2O_3 peak cannot be identified due to the trace amount partition in the alloy. The peak position of Fe-Cr is slightly shifted to the left compared with the standard peaks, which is caused by the lattice distortion due to the formation of a solid solution of Cr and Al elements with Fe [48]. Fig. 1(e) and Fig. 1(f) shows the resultant plots of the EBSD with grain boundaries clearly be observed in the backscattered SEM images. It shows that the phase structure is BCC structure without any preferential orientation, and the mean grain sizes were calculated to be 6.28 μm from the EBSD pattern (Fig. 1(d)).

2.2. Dynamic corrosion of the alloys under high-temperature LBE eutectic solution

The tests were performed in a dynamic Pb-Bi corrosion experiment apparatus with a self-assembled dissolved oxygen sensor (Bi/Bi_2O_3). Fig. 2 shows the schematic diagram of the test equipment. The autoclave was made of 316 L stainless steel with a capacity of 5 L (140 mm in inner diameter and 280 mm in depth). 3 L LBE (Shandong Hangyan New Materials Co.) was added to the autoclave during corrosion exposure tests. The temperature of the LBE in the autoclave is controlled by an electrically heated furnace at a temperature of 550 °C. Ar was introduced to control oxygen in low-concentration environments; the composition of LBE alloy used in the present work is 44.5 wt% Pb and 55.5 wt% Bi. The concentration of the dissolved oxygen in the liquid lead was measured by an oxygen sensor consisting of a saturated Bi/Bi_2O_3 reference electrode and a Mo working electrode. Oxygen content control using Ar/H_2 gas by calibrating the voltage in saturated oxygen state and oxygen-free state through the oxygen sensor, followed by fitting the relationship between voltage and oxygen content. The oxygen content can then be controlled at level of 1×10^{-4} wt%~5×10^{-4} wt% through Ar/H_2 gas [49]. The distance L from the sample to the propeller axis was measured as 50 mm (Fig. 2(b)), and the lead-bismuth flow velocity was determined via Ansys Fluent (Ansys 2022 R2), reaching 1 m/s at 600 rad/min propeller speed at the sampling point (Fig. 2(c)). It can be concluded that the sample was impacted by lead-bismuth with a flow velocity of 1 m/s. The specimens were taken out to analyze the oxide films at 500 h, 1000 h, 1500 h, and 2000 h time interval; the LBE was not replaced until the end of the entire experiment (2000 h exposure).

2.3. Microstructure characterization

The microstructure evolution of the alloy post corrosion under different time regimes was characterized by SEM (TESCAN LYRA3 GM, CZ) and EDS system (Oxford system, the UK), while the cross-section of the sample coupons was first embedded into the epoxy resin, followed by polishing it before characterization. The crystalline structure and texture property of the as-fabricated alloy were further characterized by XRD (PANalytical, NL) and EBSD (Oxford C-nano). The nanoscale information of the surface oxidation film and alteration layer was studied by STEM (FEI Tecnai G2 F20 S-TWIN). The surface roughness of the oxidation film after dynamic lead-bismuth corrosion was observed by AFM (Dimension ICON).

2.4. oxidation weight gain

The samples were weighed at corrosion intervals of 0 h,500 h,1000 h,1500 h and 2000 h. The lead-bismuth adhering to the surface of the corroded sample coupons was cleaned followed the standard protocol using a lead-bismuth cleaning solution (V(CH_3COOH): V(H_2O_2): V(C_2H_5OH) = 1:1:1) [50,51] prior to weighing, followed by ethanol cleaning before weighing. Three groups of parallel sample coupons were weighed and the average value was determined. Due to the strong adhesion of the oxide film of the samples.

2.5. Finite elemental analysis of the structural evolution of the oxidation film

Stress corrosion cracking results in the formation of minor cracks and cavities on the surface of the material, which will further nucleate and expand under external loads, leading to material damage. In finite element simulations, the Gurson-Tvergaard-Needleman (GTN) model is often used to simulate the nucleation and expansion of cracks and cavities that lead to ductile damage in metals [52,53]. The yield function of the GTN damage model is mathematically described as

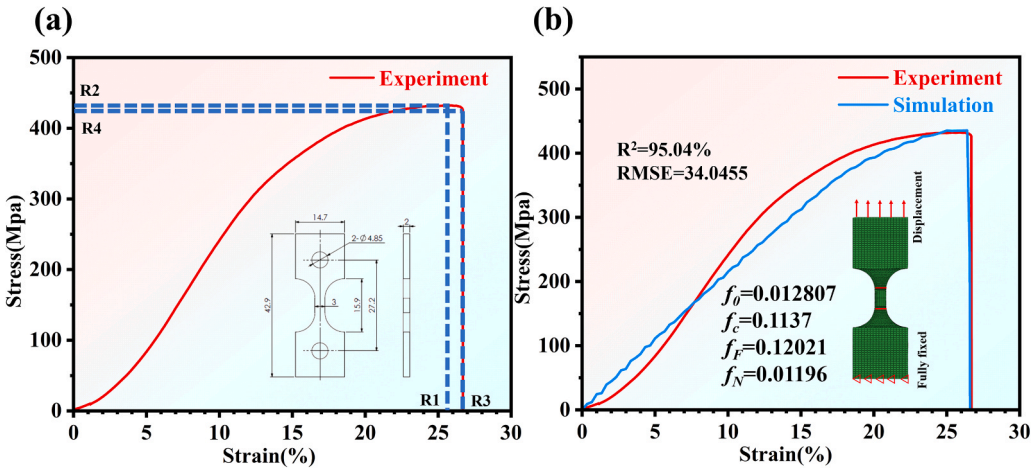

Fig. 3. (a) Experimental stress-strain curve of ODS-FeCrAl alloy at 550 °C; (b) Simulated and experimental stress-strain curves for ODS-FeCrAl alloy at 550 °C.

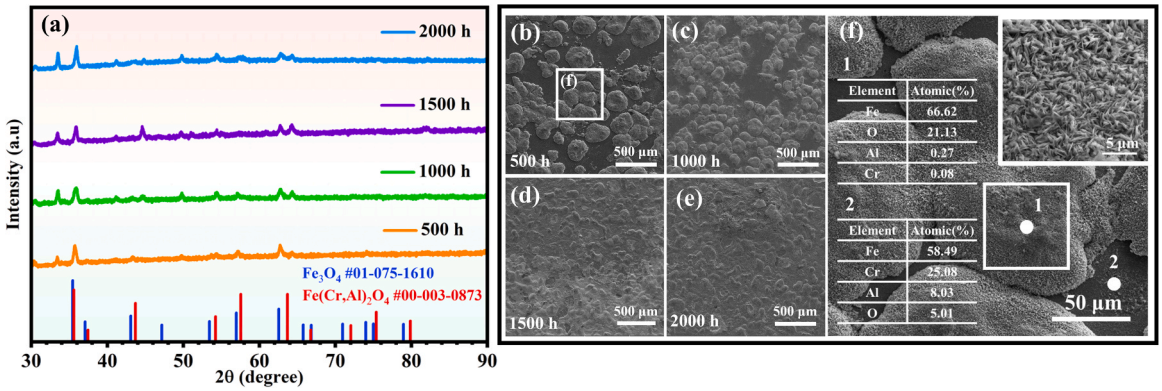

Fig. 4. (a)XRD spectra of ODS-FeCrAl samples after corrosion; (b-e) Surface microstructure of the sample surface after different corrosion times; (f) Enlarged view of the convex compound and the percentage of elements at different positions.

$$\phi = \left(\frac{\sigma_e}{\sigma_y}\right)^2 + 2q_1 f^* \cosh\left(\frac{3q_2\sigma_m}{2\sigma_y}\right) - 1 - q_3(f^*)^2 = 0 \quad (1)$$

In the equation, q_1,q_2, and q_3 are correction factors [54]; f_c represents the critical void volume fraction, at which point voids begin to coalesce; f_F denotes the void volume fraction at which the material has failed. At this point, $f^*_u = 1/q_1$, f^*_u denotes the damage variable, which is a function of the pore volume fraction. f^*_u is defined as

$$f^* = \begin{cases} f, f \le f_c \\ f_c + \dfrac{f_u^* - f_c}{f_F - f_c}(f - f_c), f_c < f \end{cases} \quad (2)$$

The GTN mesoscopic damage model requires the determination of eight damage parameters. Among these, the initial void volume fraction f_0, the critical void volume fraction f_c, the failure void volume fraction f_F, and the nucleation volume fraction f_N can be established by comparing numerical simulation results with experimental data. For the other two parameters, the average equivalent plastic strain ε_n and the nucleation strain standard deviation S_n, values of ε_n= 0.3 and S_n= 0.1 are generally applicable for most materials. q_1= 1.5, q_2= 1.0, and q_3=q_1^2 lead to excellent predictive performance of the GTN model in terms of damage as for the correction coefficients q_1, q_2 and q_3 [55]. This study employs the response surface methodology to calibrate the four parameters, including f_0. Finite element numerical simulations are performed at key points along the continuously approaching curves based on the stress-strain curves obtained from tensile tests (Fig. 3(a)). The four key values of the characteristic points in the stress-strain curve, the highest point strain R1, the highest point stress R2, the rupture point strain R3, and the rupture point stress R4 (Fig. 3(a)), are used as the response values. The GTN model parameters f_0, f_c, f_F, and f_N were used as four influencing factors to design 28 sets of unidirectional tensile simulations, and finite element simulations of uniaxial tensile tests were carried out by finite element modeling(Fig. 3(b)).Ultimately, the values of the four parameters are derived through back-calculation.

The optimal f_0, f_c, f_F, f_N are obtained by the response function, with the corresponding factors determined as f_0= 0.012807, f_c= 0.1137, f_F= 0.12021, and f_N= 0.01196, respectively. The stress-strain curve obtained from the FEA simulation is well aligned with the experimental result with R^2= 95.04 % (Fig. 3(b)).

3. Result

3.1. Microstructure evolution of the surface alteration layer

The XRD characterization of the surface of the sample after 500 h, 1000 h, 1500 h, and 2000 h dynamic lead-bismuth corrosion is shown in Fig. 4(a). The composition of the surface oxides is mainly dominated by the oxides of Fe, Cr, and Al, including the Fe_3O_4 (PDF 75–1610) and Fe (Cr, Al)$_2O_4$ (PDF 03–0873). The Al_2O_3 phase was not detected in the XRD pattern.

The surface exhibits numerous globular oxide nodules with partial curling and wrinkling on the surface of the corroded sample coupons post-corrosion in dynamic lead-bismuth with flow rate of 1 m/s. A fine needle-like structure with Fe-enriched can be seen in Fig. 4(f), which can be indexed as iron oxide. The flake iron oxide with spinel structure were

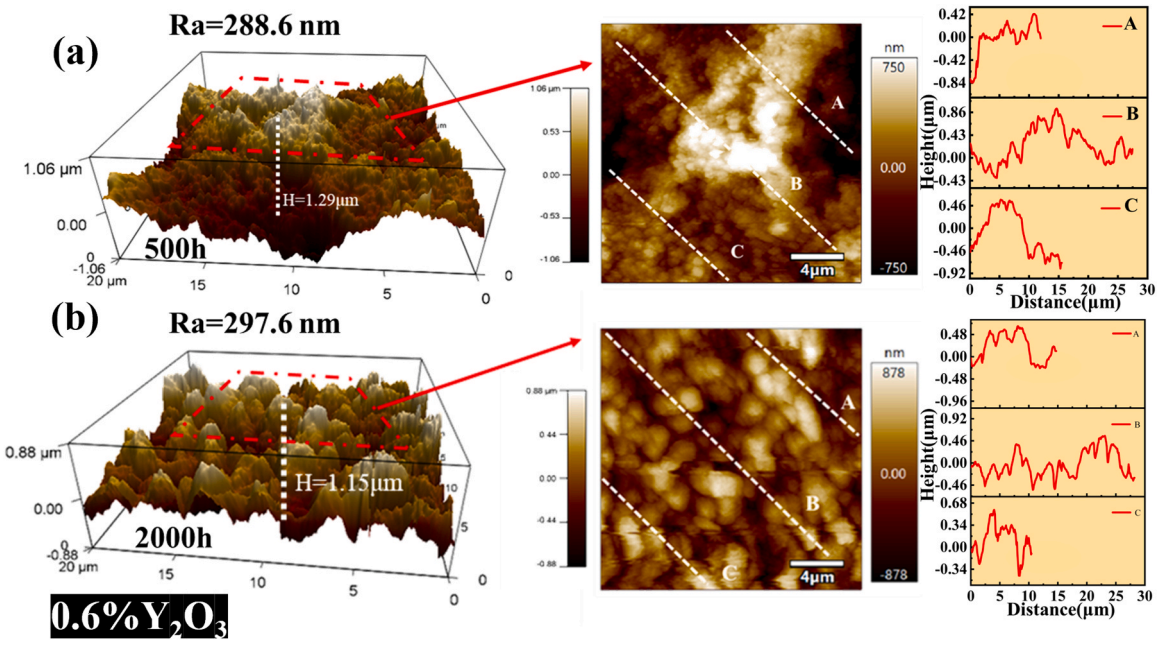

Fig. 5. (a) Surface roughness analysis of the sample surface after 500 h of corrosion; (b) surface roughness analysis of the sample surface after 2000 h of corrosion.

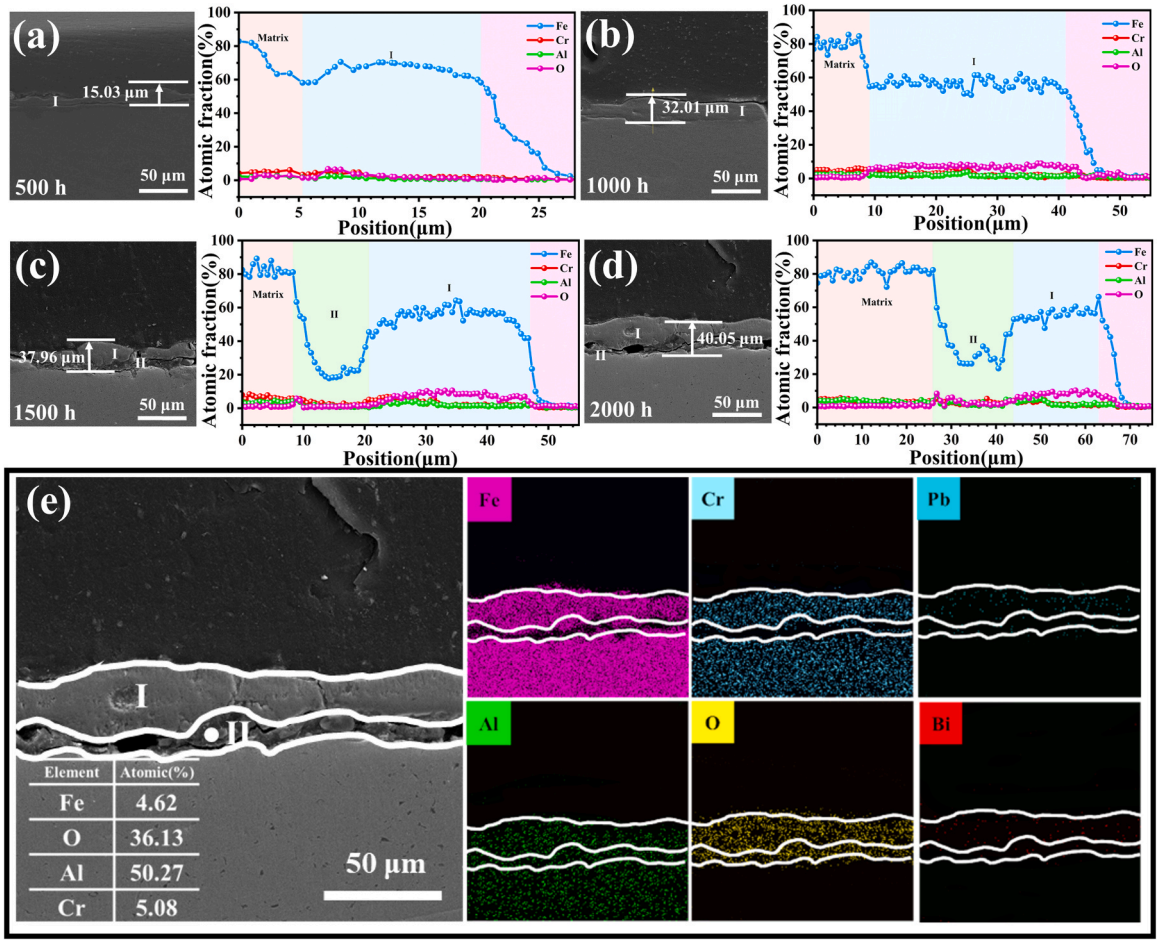

Fig. 6. (a-d) Cross-section micro structure morphology and elemental line scanning of samples post different sampling regimes; (e) EDS elemental mappings of the cross-section of the alteration layer.

Table 2
Oxide layer thickness and substance at different corrosion periods.

Time	Area (I)	Thickness	Area (II)	Thickness
500 h	Fe(Cr,Al) spinel	15.03 μm	\	0
1000 h	Fe(Cr,Al) spinel	32.01 μm	\	0
1500 h	Fe(Cr,Al) spinel	32.11 μm	Al_2O_3	5.85 μm
2000 h	Fe(Cr,Al) spinel	33.01 μm	Al_2O_3	7.04 μm

then clustered together to form spherical clusters [34,56]. The globular oxide nodules on the surface of the ODS-FeCrAl sample was Fe_3O_4 with a trans-spinel structure (Fig. 4(f)). Fe_3O_4 was the primary oxide formed by ODS-FeCrAl corrosion, as shown by the XRD results. The oxide particle is enriched in Fe and O, with the Fe and O composed of 66.62 % and 21.13 % separately according to the elemental point scanning. Correspondingly, the matrix underneath the oxide layer is enriched in Fe, Cr, Al, and O, with the corresponding semi-quantitative result denoted in Fig. 4(e).

The surface topographic information of the sample post 500 h and 2000 h corrosion test was characterized by AFM (Fig. 5). The surface roughness were 288.6 nm and 297.6 nm, corresponding to the 500 h and 2000 h, respectively. The surface post-corrosion was covered by a layer of oxidation film with a height difference of around 10 nm across a surface range of about 290 nm. The verisimilar thickness and roughness property for samples post-corrosion at 500 h and 2000 h suggests that simultaneous growth and defoliation occurred for the oxidation film during the corrosion process.

The cross-section of the oxide film/matrix interface can be seen in Fig. 6. A dense oxidation film covered on the sample surface, featuring a multiple-layer structure which can be divided into two distinguishable layers, with the Fe-enriched in the outer layer and an inner layer dominated by a Fe-leaned layer (Fig. 6(a-d)) for the sample oxidized for 1500 h to 2000 h. For comparison, a single oxide layer can be seen for the sample coupons subjected to LBE at 500 h and 1000 h. The thickness of the oxide layer and the materials at different corrosion stages are shown in the Table 2. Fig. 6(e) shows the EDS elemental semi-quantitative analysis of the cross-section, which clearly indicates that (I) area is dominated by Fe and O, with trace amount of Cr and Al existed. It can be seen that the elements Al and O make up the majority of the (II) area as shown in Fig. 6(e).

The (I) area consists of dense Fe(Cr, Al) spinel compounds, which play a major role in protecting the substrate according to the XRD analysis. For comparison, it can be seen that the content of Fe and Cr is relatively low, and the content of Al and O elements is relatively high for area (II) Fig. 6(e).

The nanoscale structural evolution of the corrosion layer for alloy after 2000 h exposure in liquid LBE was further characterized by STEM (Fig. 7). The top several micron oxide layers can be divided into three different zones, with the nano-sized grain can be seen for the top and bottom layers, as represented in (b) and (d), while grain size of several hundred nanometers can be seen for the middle layer. The triple layer structure is enriched in Fe and Cr-oxides with black spots randomly distributed. Specifically, the black spots distributed on the grains with Al-enriched can be seen on the oxide layer, suggesting the black spot is mainly composed of Al_2O_3. Al_2O_3 generated by Al oxidation may be

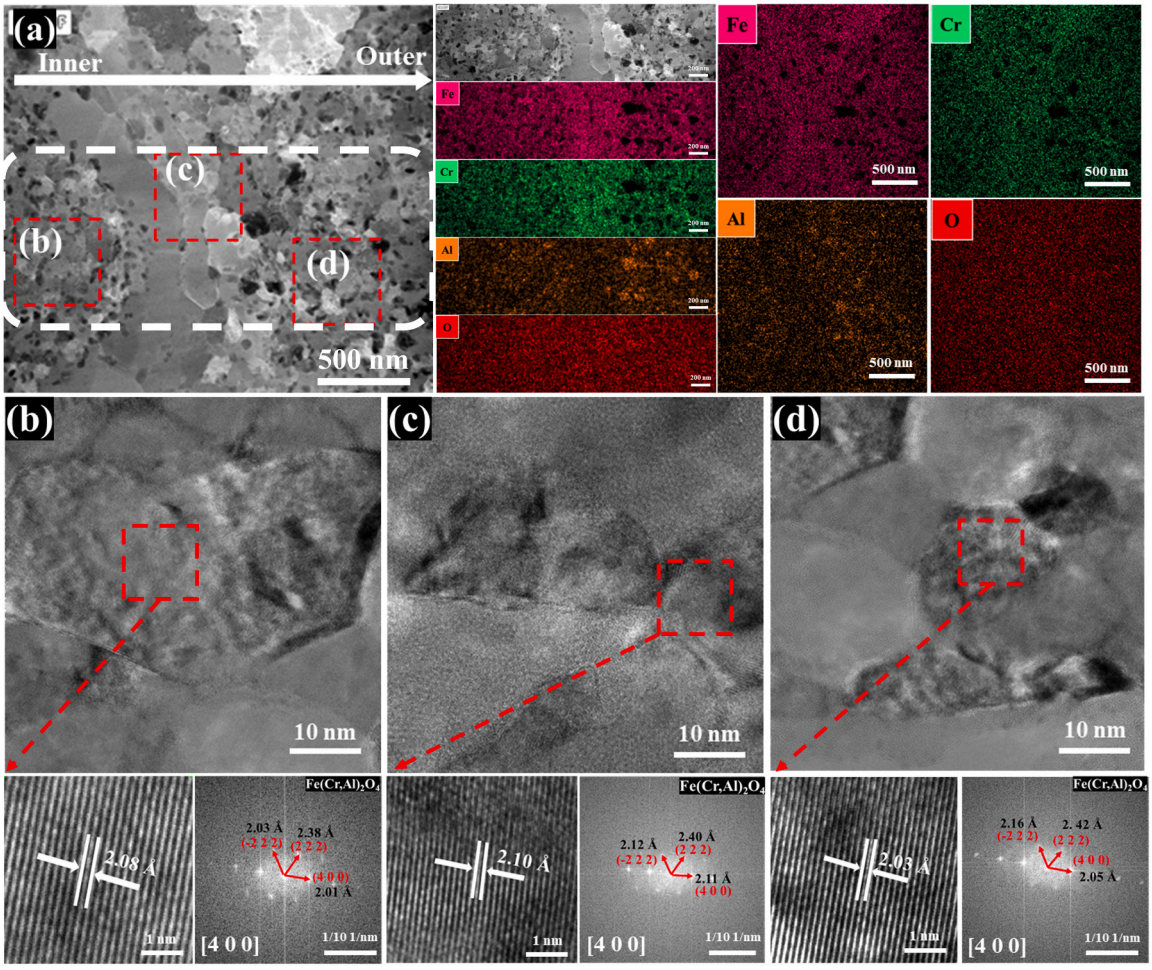

Fig. 7. Brightfield TEM image of local surface oxide film formed on ODS-FeCrAl alloy after 2000 h exposure in liquid LBE: (a) The TEM micrograph and element distribution of oxide film; (b-d) HR-TEM image and FFT diagram of the oxide films.

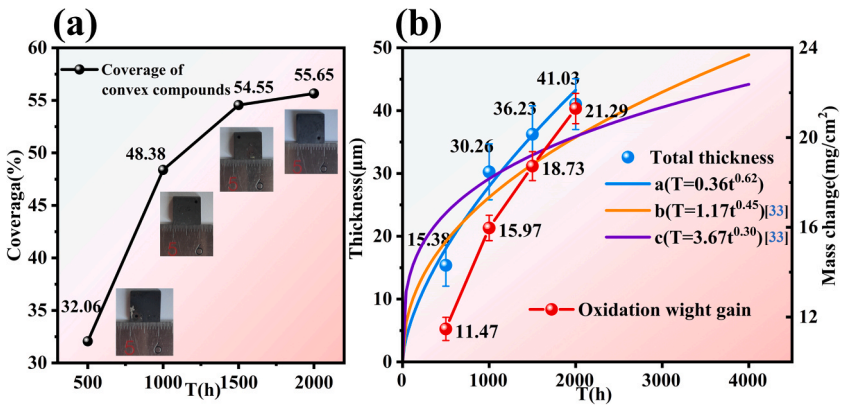

Fig. 8. (a) The surface oxidation film coverage rate as a function of time; (b) Time-dependent thickness and oxidation weight gain curves for ODS-FeCrAl.

dispersed in Fe_3O_4 in the form of tiny particles rather than forming a complete overlay. Combined with the XRD and EDS results, the Al-rich layered oxide exists in the form of $Fe(Cr, Al)_2O_4$ spinel can be seen in the XRD and EDS results (Fig. 7(b-d)), which was further evidenced by the d-spacing of 2.10 Å for the crystalline plane (400).

3.2. Growth kinetics of the surface oxidation film

The growth kinetic of the oxide film on the sample surface at different time intervals at a relative flow rate of lead-bismuth of 1 m/s is shown in Fig. 8(a). The time dependent growth of the Fe_3O_4 enriched oxide film gradually covered on the surface, with the coverage percentage increases from 32.06 % at 500 h to 55.65 % at 2000 h.

The thickness of the oxide film was measured by taking average of the several randomly selected zone on the cross-sectional of the sample coupons [10]. The time-dependent thickness of the oxide film can be fitted by a power-law model (Eq. 3) as denoted in Fig. 8(b) [15], which can then be used to predict the oxidation kinetics of ODS-FeCrAl alloys. Specifically, the thickness of the oxide film obtained from the current study (curve a) was further compared to the time dependent thickness evolution curves obtained from the literature (curves b and c) [33].

$$T = At^B \tag{3}$$

T is the oxide film thickness (μm), t is the corrosion time (h), and A and B are constants. The oxide film thickness versus time can be described as $T = 0.36\ T^{0.62}$ for a corrosion regime of 0–2000h from 15.38 μm in 500 h to 41.03 μm in 2000 h with simultaneously grow and defoliation occurred, as shown in Fig. 8(b). The oxide film thickness of ODS-FeCrAl increases dramatically at the beginning of the corrosion, which then gradually slows down as the corrosion proceeds. An initial high-speed oxidation weight gain can be attributed to the intrinsic oxidation behavior of ODS-FeCrAl alloy while shifting to a slow oxidation period with the growth of the oxidation film, which acted as the passivation film to slow down the oxygen inward diffusion.

The corresponding weight gain for the sample coupons were further denoted in Fig. 8(b). The mass change gradually increased from 11.47 mg/cm^2 in 500 h to 21.29 mg/cm^2 in 2000 h, with the corresponding decreases in growth rates due to the passivating effect of the oxide film, which shows an overall outward trend, which show good consistence with the growth trend of the thickness of the oxide film.

3.2.1. Geometric description and boundary conditions of the oxide film

The model of the surface oxidation film was constructed in ABAQUS with dimensions of 15 mm× 10 mm× 5 mm, and the model geometry meshed into discrete eight-node (CPE8RT) type elements in order to study the mechanical strength of the oxidation film subjected to

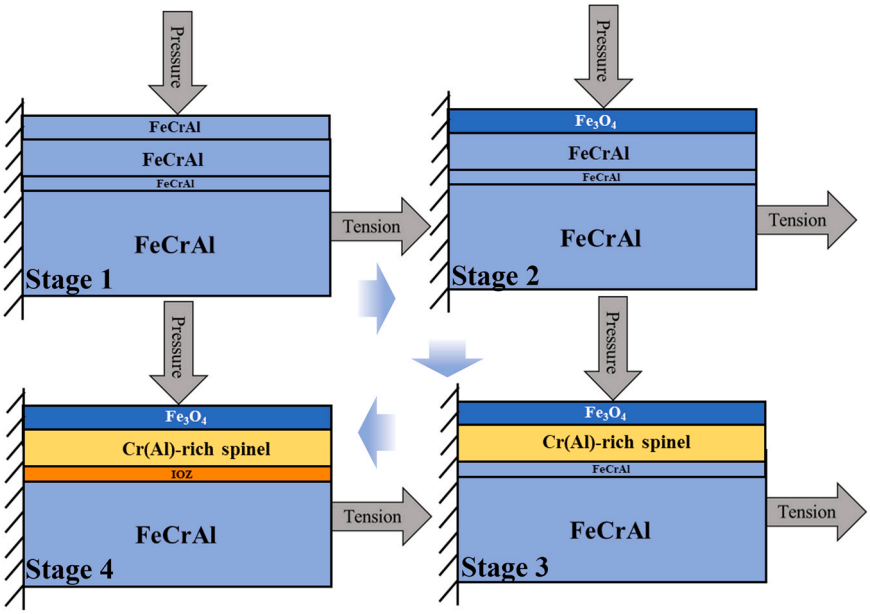

Fig. 9. Modeling of time-dependent multilayer oxide film formation.

Table 3
Basic material parameters [59–62].

Parameter	ODS-FeCrAl	Fe(Cr, Al) spinel	Fe_3O_4	Al_2O_3
Density(ρ)	7.4 g/cm^3	4.5 g/cm^3	5.17 g/cm^3	4 g/cm^3
Young's modulus(E)	2923 MPa	150 GPa	180 GPa	450 GPa
Poisson's ratio(γ)	0.3	0.25	0.28	0.3

dynamic LBE based on the actual observation in the SEM and TEM analysis in the previous section. The simulation of the real oxide film growth kinetic can be realized through dynamic altering of the material properties of the surface layer. The multilayer modeling of the matrix and oxidation layers is shown Fig. 9: Starting with a matrix alloy of ODS-FeCrAl, followed by a gradual growth of the Fe_3O_4 layer on the surface. The gradual formation of the Fe(Cr, Al) spinel oxide layer can be seen on Fe_3O_4 as the corrosion continues. The formation of the IOZ layer, i.e., the Al_2O_3 enriched oxide layer, can be seen in the final step of the oxidation. The surface roughness of the oxide film can be realized by setting a certain roughness based on the AFM analysis, which suggests an unevenly distributed Fe_3O_4.

One end of the model geometry was fixed with ENCASTRE boundary conditions, which prevented all rotational and dynamic degrees of freedom. The dynamic stretching of the oxidation film can be achieved through one end movement, while simultaneously downward pressure and rightward displacement stretching are given on the surface in order to simulate the shear stress behavior of surface oxidation film of the alloy in the LBE scenario.

The Young's modulus of magnetite, Fe(Cr,Al) spinel, and Al_2O_3 used in the current study are derived from the past researches. J.R.Nicholls measured the Young's modulus of Al_2O_3 and magnetite using the mechanical properties microprobe (MPM) technique [57], where the Young's modulus values of the Al_2O_3 ceramics were measured in the range of 419–539 GPa. The Young's modulus of the magnetite was in the range of 15l-192 GPa. Eriko Yamaki [58] measured the Young's modulus of each oxide layer by nano-indentation and find the Young's modulus of Fe–Cr spinel layer was lower than that of Fe_3O_4 layer by 10 %. Therefore, the Young's modulus of each oxide layer studied herein is shown in Table 3.

3.2.2. *Time-dependent evolution of the oxidation film*

The shear stress of the different oxide films within the different corrosion stages can be represented in Fig. 10(c). The shear stress on the Fe(Cr, Al) spinel increases sharply at the initial stage, followed by slowing down until reaching a plateau stage, with the simultaneously growth of Fe(Cr, Al) spinel and Fe_3O_4. Among these crystalline phases, Al_2O_3 suffered the highest stress, followed by Fe(Cr, Al) spinel, and Fe_3O_4 suffered the lowest stress, suggesting the Al_2O_3 exhibits robust mechanical strength compared to other oxide films (Fig. 10(d)). The highest stress is applied to the oxide layer of Al_2O_3, with the second

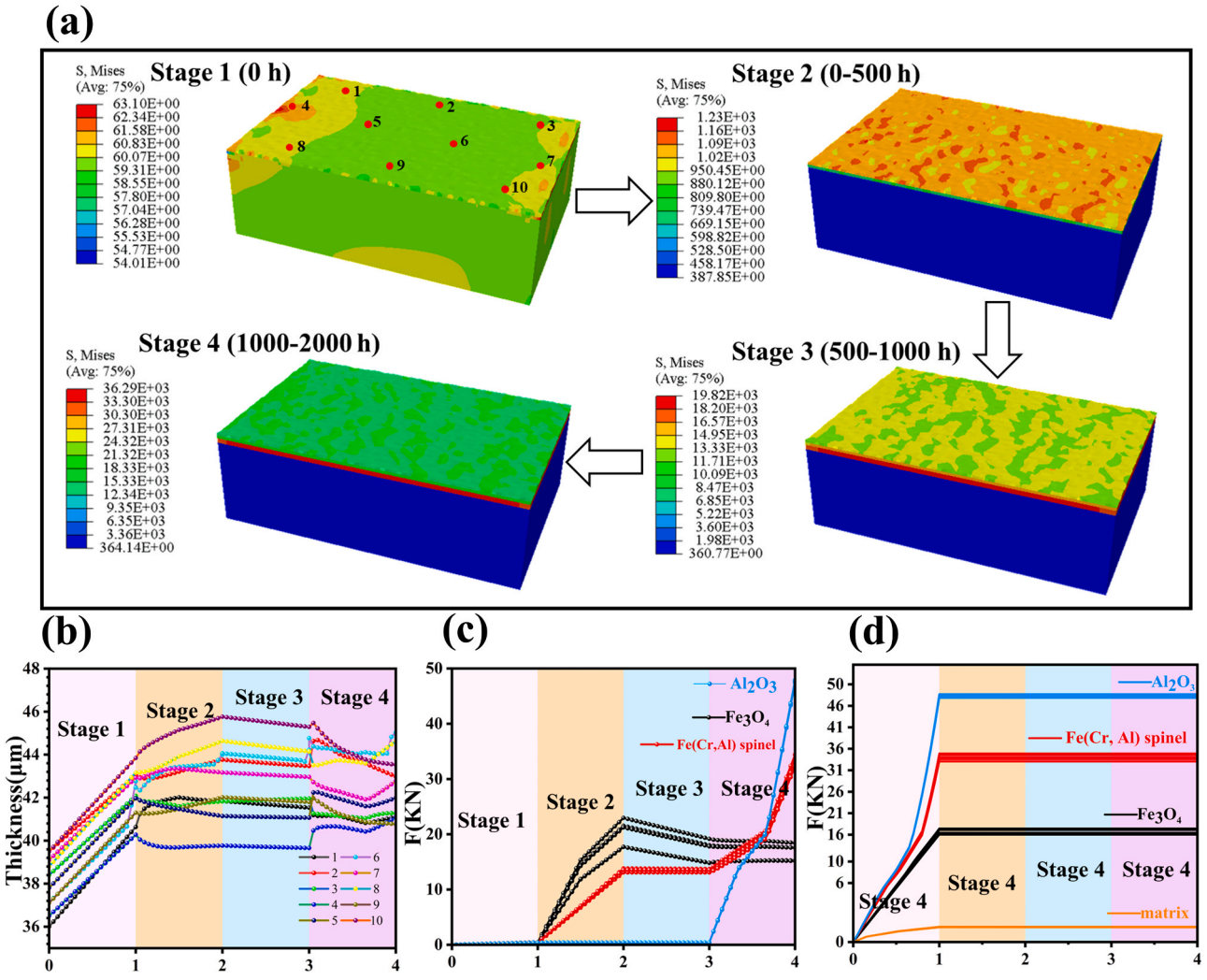

Fig. 10. (a) Finite element modeling of global stress variation in the formation of oxide film on FeCrAl alloy surface; (b) Oxide film thickness versus time; (c) Simulation results of force over time on different oxide layers; (d) Stresses results after formation of the three oxide layers.

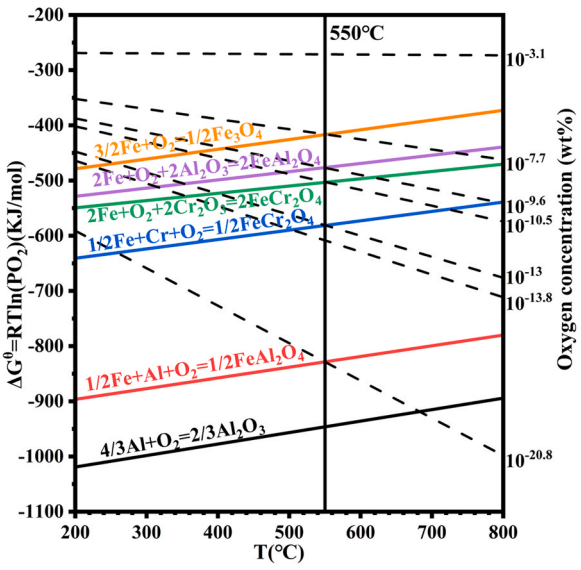

Fig. 11. Gibbs free energy vs temperature diagram of metal oxides formation [5,33].

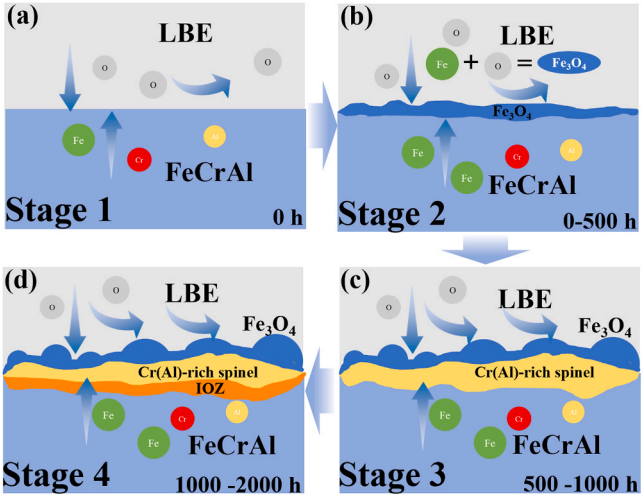

Fig. 12. Schematic diagram of multilayer oxide film formation of ODS-FeCrAl alloy under dynamic LBE corrosion (time dependent).

stress is applied to the layer of Fe(Cr, Al) spinel, and the minimum stress is applied to Fe_3O_4 for the final stage of the growth of the oxide film (Fig. 10(d)). The self-generated Al_2O_3 oxide film is better than other oxide layers in terms of mechanical properties, resulting in the superior reliability and corrosion resistance for ODS-FeCrAl alloy. Moreover, since the oxide layer absorbs a lot of mechanical impact, the impulse force on the matrix is much smaller than that on the oxide layer, suggesting the shielding effect of oxide film on the matrix as shown in Fig. 10(d). Overall, the above results indicate that the ODS-FeCrAl alloy is more resistant to impact with the formation of oxide film on the sample surface, which further confirms the protective ability of the film.

4. Discussion

4.1. Time-dependent growth and structural evolution of the oxidation film

The surface alteration and structural evolution of the oxide film of alloy subjected to LBE is highly dependent on temperature, oxygen concentration, and the properties of the elements themselves (Gibbs free energy change, ΔG) [18,19,63]. The standard ΔG (per one mol of O_2 consumed) for the oxide formation relating to the main constitutive elements of the ODS-FeCrAl alloy as a function of temperature can then be calculated and plotted in Fig. 11. From a thermodynamic point of view, the stable existence of oxides depends on oxygen concentrations with Fe_3O_4, $FeCr_2O_4$, $FeAl_2O_4$ and Al_2O_3 can be stabilized in the FeCrAl alloy exposed in 550 ℃.

The multilayer oxide film growth mechanism of ODS-FeCrAl sample coupons subjected to dynamic LBE environment in the current study can be explained by the element diffusion mechanism model proposed by Martinelli and Muller based on the above characterization and the thermodynamic calculation results [5,64,65]. Dynamic growth and defoliation of oxide film due to the mechanical stress and eutectic dissolution of surface oxide film into the eutectic LBE can be seen for the alloy subjected to LBE [41]. The microstructure evolution mechanism of the oxide film in LBE can then be summarized in the following schematic diagram (Fig. 12). The continuous dissolution of Fe from the alloy into the LBE left a large number of vacancies on the surface of the matrix, which gradually accumulated into “micropores” on the surface of the matrix [39]. Partial of the Fe simultaneously reacted with the rare oxygen in the LBE to form the outer layer enriched in Fe_3O_4, followed by inward diffusion of oxygen to react with the Fe and Cr, Al atoms near the surface of the matrix through the formation of “microporous channels” to form Fe(Cr, Al) spinel oxides, as shown in Fig. 12(c) [12,65–67]. Generally, the double-layer oxide film formed in LBE is composed of magnetite and Fe-Cr spinel due to the outward diffusion of Fe and simultaneously the inward diffusion of O [67]. The presence of the Fe (Cr, Al) oxide layer provides a fast pathway for the diffusion of the surrounding matrix elements and the penetration of the O [65]. It is widely recognized that the samples will be more susceptible to the shear stress result from the LBE flow, and the stress prompts an increase in the structural defects in the Fe(Cr, Al) spinel layer, which enhances the acceleration of the diffusion of Fe outward, thus increasing the oxidative corrosion rate [68,69].

Compare to the alloys corroded in static lead-bismuth environment, the oxidation weight gains and thickness of the oxide film in dynamic lead-bismuth environment are higher as denoted in the weight gain curves in Fig. 8(b). The growth of the surface oxide film is more aggressive as the film thickness of 40 μm can be seen for the alloy corroded for 2000 h, while more than 4000 h is needed in static lead-bismuth environment [33]. The dynamic liquid LBE can accelerate oxidation corrosion by further enhancing the growth of the surface oxidation film due to the increases in mass transportation along the solid/liquid interface [69,70]. Moreover, the mechanical shear stress exert significant stripping forces on the developing oxide film of Fe_3O_4, which promotes the formation of locally unstable oxide structures, which demonstrates distinguishable morphology as compared to the alloys subjected to static LBE (Fig. 4(b-e)) [33]. In addition, the addition of Y_2O_3 can enhance the adhesion between the oxide scale and the substrate by suppressing the outward diffusion of metal cations and altering grain boundary diffusion kinetics, further promoting the formation of a more coherent and adherent Al_2O_3 oxide layer [31,32].

The diffusion of oxygen and Fe atom can be deterred with the reduction of the corrosion rate of ODS-FeCrAl alloy with the increasing growth of the oxide film, results in the transition of oxidation kinetic from initial fast dissolution to film diffusion (Fig. 8(b)). A Fe depletion zone occurs at the spinel layer/matrix interface, where O ions diffused into the matrix to react with Al ions to form Al-rich oxides simultaneous with the growth of the spinel, and final Al_2O_3 grows inward to form a continuous protective layer. The oxide film acted as a physical barrier to limit the diffusion of cations required for the growth of the outer layer, which further leads to a slow oxidation rate (Fig. 12(d)). Meanwhile, the XRD peaks for the Al_2O_3 cannot be detected, probably can be attributed to the surface covered by layers of Fe(Cr, Al) spinel and Fe_3O_4 oxides above as denoted by the cross-section TEM analysis (Fig. 4(a)).

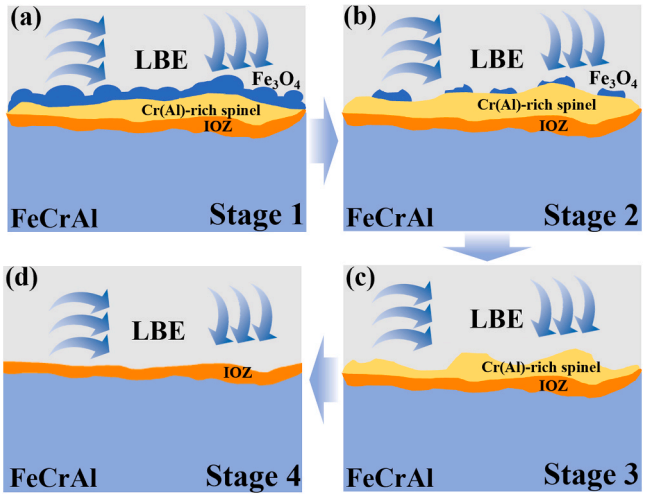

Fig. 13. Schematic diagram of the surface oxide film defoliation subjected to the different LBE corrosion regimes (time dependent).

4.2. Correlation between oxidation film heterogeneity and structural stability

The surface roughness gradually increases with the growth of the surface oxidation film, with the distribution of surface stress gradually turns out to be inhomogeneous according to the FEA analysis. The point-like surface stress aligns well with the evolution of the surface alteration layer microstructure (Fig. 10(a)). Therefore, the protective capability of the surface oxide film is highly dependent on the film structural integrity, with the shear stress likely to accumulate on the area with film defoliation. The gradual shear stress accumulation on the area without film further accelerates the film cracking and defoliation. The mathematical modeling result is consistent with the experimental observation that the film growth rate is higher at the initial stage, which then slows down in the later stage.

On the other hand, it is suggested that Al_2O_3 is subjected to the greatest stress, featuring high densities of Al_2O_3, strong adhesion, and high Young's modulus. For comparison, magnetite and Fe(Cr, Al) spinel are in the outward layer of the oxide film, which is easily scoured away by the LBE (Fig. 13). Therefore, the Al_2O_3 layer is critical to the improvement of the mechanical strength of the surface oxide film so as to enhance the resistance in LBE. Overall, the anti-corrosive ability of ODS-FeCrAl alloy to dynamic LBE has strong correlation with the formation of Al_2O_3, which can be used to guide the design of the alloy by optimizing the chemical composition and microstructure of the alloy in order to enhance the formation of Al_2O_3.

5. Conclusions

The current study mainly focuses on the surface alteration and oxide film behavior of self-assembled ODS-FeCrAl alloy subjected to dynamic LBE with controlled dissolved oxygen by combining experimental and numerical modeling. The main conclusions are as follows:

(1) A triple oxide layer structure can be found for the ODS-FeCrAl alloy subjected to long-term eutectic LBE flow. The time-dependent chemical composition and microstructure evolution of the film can be revealed. The oxide layer with Fe_3O_4 enriched is formed at the initial stage of the oxidation, followed by the formation of a dense structure of Fe(Cr, Al) spinel oxide with the continuous interaction with LBE. At the late stage of oxidation, a small amount of Al_2O_3 oxide forms staying in the bottom of the oxide layer with the time-driven growth of oxide film.

(2) The corrosion and oxide film growth rate in the dynamic lead-bismuth environment is faster compared with the alloy corroded in the static lead-bismuth environment. The surface morphology of the oxide film featured with curled oxide nodules under dynamic LBE is significantly different from the dense and uniform oxide film usually formed under static conditions.

(3) The triple layer structure of the oxide film demonstrates heterogeneous shear stress resistance with the Al_2O_3 suffers the highest shear stress, which is critical to the anti-corrosive behavior of the ODS-FeCrAl alloy, followed by Fe(Cr, Al) spinel.

CRediT authorship contribution statement

Liu Jiwu: Writing – original draft, Software, Resources, Investigation, Data curation. **Yang Kun:** Writing – review & editing, Supervision, Project administration, Methodology, Funding acquisition, Conceptualization. **Tang Xiaobin:** Writing – review & editing. **Sun Zhangjie:** Data curation. **Chen Feida:** Supervision, Resources. **Ru Wangwei:** Resources. **Liu Tianhao:** Investigation.

Declaration of Competing Interest

The authors declare that they have no known competing financial interests or personal relationships that could have appeared to influence the work reported in this paper.

Acknowledgements

The authors would like to express appreciation for financial support from Natural Science Foundation of Jiangsu Province (BK20230898); National Natural Science Foundation of China (No. 37244600);

Appendix A. Supporting information

Supplementary data associated with this article can be found in the online version at doi:10.1016/j.jallcom.2025.181167.

References

[1] A. AlembertI, The lead fast reactor: an opportunity for the future? Engineering 2 (1) (2016) 59–62.
[2] H. Jiang, X. Zhao, S. Cao, et al., Effect of Y2O3 addition on the microstructure and liquid LBE cavitation erosion behaviors of Fe-Cr-Al-Ti-C-xY2O3 laser clade coatings, J. Nucl. Mater. 572 (2022) 154030.
[3] W. Luo, Q. Huang, L. Luo, et al., Effect of Ce on microstructure evolution of oxide scale for CLAM steel exposed to LBE containing 10− 6wt% oxygen at 500℃, J. Nucl. Mater. 573 (2023) 154109.
[4] Fazio C., Sobolev V., Aerts A., et al. Handbook on lead-bismuth eutectic alloy and lead properties, materials compatibility, thermal-hydraulics and technologies-2015 edition, Organisation for Economic Co-Operation and Development, 2015.
[5] C. Schroer, J. Konys, Physical chemistry of corrosion and oxygen control in liquid lead and lead-bismuth eutectic, Forsch. Karlsr. Karlsr. (2007).
[6] C. Fazio, F. Balbaud, Corrosion phenomena induced by liquid metals in Generation IV reactors. Structural Materials for Generation IV Nuclear Reactors, Elsevier, 2017, pp. 23–74.
[7] O. Klok, K. Lambrinou, S. Gavrilov, et al., Effect of deformation twinning on dissolution corrosion of 316L stainless steels in contact with static liquid lead-bismuth eutectic (LBE) at 500° C, J. Nucl. Mater. 510 (2018) 556–567.
[8] A. Heinzel, A. Weisenburger, G. Müller, Corrosion behavior of austenitic steels in liquid lead bismuth containing 10− 6wt% and 10− 8wt% oxygen at 400–500° C, J. Nucl. Mater. 448 (1-3) (2014) 163–171.
[9] S. Tian, Z. Jiang, L. Luo, Oxidation behavior of T91 steel in flowing oxygen-containing lead-bismuth eutectic at 500° C, Mater. Corros. 67 (12) (2016) 1274–1285.
[10] Q. Shi, J. Liu, H. Luan, et al., Oxidation behavior of ferritic/martensitic steels in stagnant liquid LBE saturated by oxygen at 600° C, J. Nucl. Mater. 457 (2015) 135–141.
[11] V. Tsisar, C. Schroer, O. Wedemeyer, et al., Long-term corrosion of austenitic steels in flowing LBE at 400° C and 10− 7 mass% dissolved oxygen in comparison with 450 and 550° C, J. Nucl. Mater. 468 (2016) 305–312.
[12] V. Tsisar, C. Schroer, O. Wedemeyer, et al., Characterization of corrosion phenomena and kinetics on T91 ferritic/martensitic steel exposed at 450 and 550° C to flowing Pb-Bi eutectic with 10− 7 mass% dissolved oxygen, J. Nucl. Mater. 494 (2017) 422–438.

[13] V. Tsisar, C. Schroer, O. Wedemeyer, et al., Corrosion behavior of austenitic steels 1.4970, 316L and 1.4571 in flowing LBE at 450 and 550° C with 10− 7 mass% dissolved oxygen, J. Nucl. Mater. 454 (1-3) (2014) 332–342.
[14] K.L. Murty, I. Charit, Structural materials for Gen-IV nuclear reactors: challenges and opportunities, J. Nucl. Mater. 383 (1-2) (2008) 189–195.
[15] J. Zhang, A review of steel corrosion by liquid lead and lead–bismuth, Corros. Sci. 51 (6) (2009) 1207–1227.
[16] A.L. Johnson, D. Parsons, J. Manzerova, et al., Spectroscopic and microscopic investigation of the corrosion of 316/316L stainless steel by lead–bismuth eutectic (LBE) at elevated temperatures: importance of surface preparation, J. Nucl. Mater. 328 (2-3) (2004) 88–96.
[17] M. Caro, K. Woloshun, F. Rubio, et al., Heavy liquid metal corrosion of structural materials in advanced nuclear systems], Jom 65 (2013) 1057–1066.
[18] V. Fedirko, O. Eliseeva, V. Kalyandruk, et al., Corrosion of armco iron and model Fe− Cr-Al alloys in oxygen-containing lead melts, Mater. Sci. 33 (2) (1997) 207–211.
[19] A. Weisenburger, A. Jianu, S. Doyle, et al., Oxide scales formed on Fe–Cr–Al-based model alloys exposed to oxygen containing molten lead], J. Nucl. Mater. 437 (1-3) (2013) 282–292.
[20] D. Frazer, E. Stergar, C. Cionea, et al., Liquid metal as a heat transport fluid for thermal solar power applications, Energy Procedia 49 (2014) 627–636.
[21] N. Li, Active control of oxygen in molten lead–bismuth eutectic systems to prevent steel corrosion and coolant contamination, J. Nucl. Mater. 300 (1) (2002) 73–81.
[22] J. Zhang, Oxygen control technology in applications of liquid lead and lead–bismuth systems for mitigating materials corrosion, J. Appl. Electrochem. 43 (2013) 755–771.
[23] C. Cionea, M. Abad, Y. Aussat, et al., Oxide scale formation on 316L and FeCrAl steels exposed to oxygen controlled static LBE at temperatures up to 800° C, Sol. Energy Mater. Sol. Cells 144 (2016) 235–246.
[24] D. Wang, S. Liu, X. Ma, et al., Enhanced corrosion resistance of 15–15Ti austenitic steel in liquid lead-bismuth eutectic at 550℃ by shot peening processing, Corros. Sci. 226 (2024) 111640.
[25] D. Wang, S. Liu, C. Xiao, et al., Corrosion resistance of 15–15Ti and 316Ti austenitic steels as fuel cladding in liquid lead-bismuth eutectic at 550℃: the dominant role of grain structure, Corros. Sci. 218 (2023) 111169.
[26] S. Liu, W. Zhu, Y. Li, et al., New insights into selective leaching and ferritization in 15-15Ti austenitic steel in lead-bismuth eutectic through parent phase reconstruction, Scr. Mater. 254 (2025) 116316.
[27] F. Stott, G. Wood, J. Stringer, The influence of alloying elements on the development and maintenance of protective scales, Oxid. Met. 44 (1995) 113–145.
[28] C. Wagner, Passivity and inhibition during the oxidation of metals at elevated temperatures, Corros. Sci. 5 (11) (1965) 751–764.
[29] Z. Zhang, X. ZhanG, L. Sheng, et al., The effect of the third element Cr on oxidation behavior of Fe-xCr-10Al (at%) alloys at 900C, Open Corros. J. 2 (1) (2009).
[30] K.A. TerranI, B.A. Pint, Y.-J. Kim, et al., Uniform corrosion of FeCrAl alloys in LWR coolant environments, J. Nucl. Mater. 479 (2016) 36–47.
[31] D. Naumenko, B.A. Pint, W. Quadakkers, Current thoughts on reactive element effects in alumina-forming systems: in memory of John Stringer, Oxid. Met. 86 (2016) 1–43.
[32] T. Huang, J. Lü, P. Song, et al., Effect of Pt doping on oxide scale formation on yttria-dispersion FeCrAl alloy at 1200℃, Corros. Sci. 168 (2020) 108580.
[33] Z. Zhu, J. Tan, X. Wu, et al., Corrosion behaviors of FeCrAl alloys exposed to oxygen-saturated static lead bismuth eutectic at 550° C, Corros. Sci. 209 (2022) 110767.
[34] H. Wang, G. Liang, C. Meng, et al., A comparative study on the corrosion performance of four FeCrAl alloys with different Cr contents in contact with oxygen-saturated LBE, J. Mater. Res. Technol. 23 (2023) 3492–3504.
[35] N. Liu, Y. Cui, Y. Zhang, et al., Effects of Zr addtion on recrystallization behaviors and mechanical properties of FeCrAl alloys, J. Mater. Res. Technol. 22 (2023) 393–402.
[36] C. Kim, C. Tang, M. Grosse, et al., Oxidation mechanism and kinetics of nuclear-grade FeCrAl alloys in the temperature range of 500–1500C in steam, J. Nucl. Mater. 564 (2022) 153696.
[37] C. Xue, Z. Zhang, J. Tan, et al., Effects of Zn injection on corrosion behavior and crud deposition of FeCrAl fuel cladding under subcooled nuclear boiling condition in high-temperature pressurized water, Corros. Sci. 211 (2023) 110909.
[38] R.B. Rebak, T.B. Jurewicz, M. Larsen, et al., Zinc water chemistry reduces dissolution of FeCrAl for nuclear fuel cladding, Corros. Sci. 198 (2022) 110156.
[39] J. Ejenstam, M. Halvarsson, J. Weidow, et al., Oxidation studies of Fe10CrAl–RE alloys exposed to Pb at 550C for 10,000h, J. Nucl. Mater. 443 (1-3) (2013) 161–170.
[40] Z. Yang, J. Pan, Z. Wang, et al., New insights into the mechanism of yttrium changing high-temperature oxide growth of Fe-13Cr–6Al–2Mo–0.5Nb alloy for fuel cladding, Corros. Sci. 172 (2020) 108728.
[41] Mudali U.K., Raj B.. HIGH nitrogen steels and stainless steels: manufacturing, properties and applications [J]. (No Title), 2004.
[42] P. Hosemann, R. Dickerson, P. Dickerson, et al., Transmission electron microscopy (TEM) on oxide layers formed on D9 stainless steel in lead bismuth eutectic (LBE), Corros. Sci. 66 (2013) 196–202.
[43] V. Tolpygo, D. Clarke, Spalling failure of α-alumina films grown by oxidation: I. Dependence on cooling rate and metal thickness, Mater. Sci. Eng. A 278 (1-2) (2000) 142–150.
[44] V. Vijayaraghavan, A. Garg, L. Gao, et al., Finite element based physical chemical modeling of corrosion in magnesium alloys, Metals 7 (3) (2017) 83.
[45] C. Yuheng, W. Yang, Z. Chunyu, et al., Development of a damaged viscoplasticity model with preliminary application in Zircaloy cladding material, Mech. Mater. 168 (2022) 104274.
[46] P. Nègre, D. Steglich, W. Brocks, Crack extension in aluminium welds: a numerical approach using the Gurson–Tvergaard–Needleman model, Eng. Fract. Mech. 71 (16-17) (2004) 2365–2383.
[47] A. Nonn, W. Dahl, W. Bleck, Numerical modelling of damage behaviour of laser-hybrid welds, Eng. Fract. Mech. 75 (11) (2008) 3251–3263.
[48] X. Gong, J. Chen, C. Xiang, et al., A comparative study on liquid metal embrittlement susceptibility of three FeCrAl ferritic alloys in contact with liquid lead-bismuth eutectic at 350° C, Corros. Sci. 183 (2021) 109346.
[49] J. Zhang, N. Li, Y. Chen, Oxygen control technique in molten lead and lead-bismuth eutectic systems, Nucl. Sci. Eng. 154 (2) (2006) 223–232.
[50] D. Sapundjiev, S. Van Dyck, W. Bogaerts, Liquid metal corrosion of T91 and A316L materials in Pb–Bi eutectic at temperatures 400–600° C, Corros. Sci. 48 (3) (2006) 577–594.
[51] W. Zhang, Y. Zhong, X. Qiu, et al., Screening of the FeCrAl LBE corrosion-resistant coatings: the effect of Cr and Al contents, Surf. Coat. Technol. 462 (2023) 129477.
[52] Gurson A.L. Continuum theory of ductile rupture by void nucleation and growth: Part I—Yield criteria and flow rules for porous ductile media, 1977.
[53] A. Needleman, V. Tvergaard, An analysis of ductile rupture in notched bars, J. Mech. Phys. Solids 32 (6) (1984) 461–490.
[54] V. Tvergaard, Influence of voids on shear band instabilities under plane strain conditions, Int. J. Fract. 17 (1981) 389–407.
[55] M.I.N.H. Fuguo, L. Zhigang, W. Forming, limit stress diagram prediction of aluminum alloy 5052 based on GTN model parameters determined by in situ tensile test, Chin. J. Aeronaut. 24 (3) (2011) 378–386.
[56] H.-Z. Chen, B.-R. Li, B. Wen, et al., Corrosion resistance of iron-chromium-aluminium steel in eutectic molten salts under thermal cycling conditions, Corros. Sci. 173 (2020) 108798.
[57] J. Nicholls, D. Hall, P. Tortorelli, Hardness and modulus measurements on oxide scales, Mater. High. Temp. 12 (2-3) (1994) 141–150.
[58] E. Yamaki, K. Kikuchi, A stability of oxide layers formed in LBE on HCM12A to external loading, J. Nucl. Mater. 398 (1-3) (2010) 153–159.
[59] M.R. Gallas, G.J. Piermarini, Bulk modulus and Young's modulus of nanocrystalline γ-alumina, J. Am. Ceram. Soc. 77 (11) (1994) 2917–2920.
[60] D. Chicot, J. Mendoza, A. Zaoui, et al., Mechanical properties of magnetite (Fe3O4), hematite (α-Fe2O3) and goethite (α-FeO· OH) by instrumented indentation and molecular dynamics analysis, Mater. Chem. Phys. 129 (3) (2011) 862–870.
[61] K.G. Field, M.A. Snead, Y. Yamamoto, et al., Handbook on the material properties of FeCrAl alloys for nuclear power production applications, Nucl. Technol. Res. Dev. (2017).
[62] J. Zhang, Long-term behaviors of oxide layer in liquid lead–bismuth eutectic (LBE), Part I: model development and validation, Oxid. Met. 80 (5) (2013) 669–685.
[63] J. Ejenstam, M. Thuvander, P. Olsson, et al., Microstructural stability of Fe–Cr–Al alloys at 450–550C, J. Nucl. Mater. 457 (2015) 291–297.
[64] G. Müller, G. Schumacher, F. Zimmermann, Investigation on oxygen controlled liquid lead corrosion of surface treated steels, J. Nucl. Mater. 278 (1) (2000) 85–95.
[65] L. Martinelli, F. Balbaud-Célérier, A. Terlain, et al., Oxidation mechanism of a Fe–9Cr–1Mo steel by liquid Pb–Bi eutectic alloy (Part I), Corros. Sci. 50 (9) (2008) 2523–2536.
[66] O. Yeliseyeva, V. Tsisar, G. Benamati, Influence of temperature on the interaction mode of T91 and AISI 316L steels with Pb–Bi melt saturated by oxygen, Corros. Sci. 50 (6) (2008) 1672–1683.
[67] L. Martinelli, F. Balbaud-Célérier, A. Terlain, et al., Oxidation mechanism of an Fe–9Cr–1Mo steel by liquid Pb–Bi eutectic alloy at 470C (Part II), Corros. Sci. 50 (9) (2008) 2537–2548.
[68] G. Chen, N. Ju, Y. Lei, et al., Corrosion behavior of 410 stainless steel in flowing lead-bismuth eutectic alloy at 550° C, J. Nucl. Mater. 522 (2019) 168–183.
[69] Z. Wang, H. Chen, Flowing liquid metal corrosion of structural steels in the Pb-Bi eutectic, Adv. Mater. Res. 581 (2012) 1040–1043.
[70] G. Chen, H. Yang, H. sun, et al., Exploring the high-temperature steam oxidation behaviors of the lean-Cr (7–10wt%) FeCrAl alloys, Corros. Sci. 194 (2022) 109927.